Structure-based 3D-QSAR models and dynamics analysis of novel *N*-benzyl pyridinone as p38α MAP kinase inhibitors for anticytokine activity

Zaheer Ul-Haq *, Waqasuddin Khan, Syeda Rehana Zia, Sadaf Iqbal

Dr. Panjwani Center for Molecular Medicine and Drug Research, International Center, for Chemical and Biological Sciences, University of Karachi, Karachi-75270, Pakistan

ARTICLE INFO

ABSTRACT

A novel series of anticytokine *N*-benzyl pyridinone derivatives that targets p38α MAP kinase has been analyzed by utilizing a combination of molecular modeling techniques. Statistically significant structure-based 3D-QSAR models were generated for both CoMFA and CoMSIA, and validated through acceptable predictive ability to support both internal and external set of compounds. Structural changes within the protein key backbone residues (Met109 and Gly110), DFG loop position, and side chain movements (Lys53 and Asn114) as resulted by different substituents on these inhibitors were also examined by molecular dynamics simulation. The protocol applied in this study could be helpful to rationalize potent compounds with better inhibitory activity and selectivity profiles against p38α MAP kinase.

1. Introduction

Mammalian mitogen-activated protein (MAP) kinases (EC 2.7.11.24), a group of serine/threonine kinases, mediate intracellular signal transduction pathways [1,2]. MAP kinases are classified on the basis of divergence found in their sequences and activation loop that categorizes them into four other kinases; extracellular signal-regulated kinases (ERKs), c-Jun N-terminal kinases (JNKs) or stress-activated protein kinases (SAPKs) and p38 MAP kinases. MAP kinases are activated in response to bacterial liposaccharides, inhibitors of protein synthesis [3–5], and some other parameters that include ultraviolet radiation (physical) and cellular stresses (chemical or heat shock).

p38 MAP kinases belong to a family of proline-directed serine/threonine kinases, and have been identified as a central kinase in the stress induced MAPKAP pathways [6,7]. The activation loop of p38 MAP kinases is catalytically inactive and remains unphosphorylated in the absence of stress–response signaling. Upon activation by upstream kinases (MKK3 and MKK6 [8]), dual phosphorylation occurs on both Thr180 and Tyr182 residues (in case of p38α MAP kinase) of activation loop located in close proximity to the ATP and substrate binding sites. This activation leads to subsequent signaling of a wide variety of downstream pathways including the cytokine production cascade, and other transcriptional factors. Significant transcriptional upregulation of TNFα and IL-1β takes place that causes persistent inflammation-induced destruction of joints and bones, a frequent and clinically serious event associated in patients with rheumatoid arthritis (RA) [9,10]. TNFα is important in early joint swelling, whereas IL-1β has a pivotal role in sustained cell infiltration and erosive cartilage damage. Cytokine blockade by diminution of downstream MAP kinase pathways is of major importance in the rapidity of reduction in pain, stiffness, swelling, and tenderness of joints [11].

Four splicing isoforms of p38 MAP kinases [p38α (MAPK14), β (MAPK11), γ (MAPK12 or ERK6) and δ (MAPK13 or SAPK4)] have been discovered with 40–60% structural homology to each other [12–15] while the functionality of p38β, p38γ and p38δ have yet to be identified [16]. Over the past years several promising targets for the treatment of arthritic bone destruction have been defined [17,18]. Quite a few reports indicate that activation of p38α MAP kinase has an insightful role in several inflammatory and autoimmune diseases such as rheumatoid arthritis (RA), osteoporosis, Chrohn's disease [19], inflammatory bowel disease, toxic shock syndrome and psoriasis. In vivo anti-inflammatory activity has been observed for several rodent models that designated p38α MAP kinase as a valid drug target. Clinical data obtained with either chimeric TNFα antibody [20–23] or soluble TNFα receptor [24] in the treatment of RA and Chrohn's disease has further confirmed the upregulation of TNFα in these inflammatory conditions. The blockade of proinflammatory cytokine biosynthesis (such as TNFα, IL-1β, IL-5 and IL-8) has become possible via the inhibition of p38α MAP kinase by the development of small molecules in monocytic cell systems [25].

* Corresponding author. Tel.: +92 21 111 222 292x309; fax: +92 21 481 901 819.
E-mail addresses: zaheer.qasmi@iccs.edu, zaheer_qasmi@hotmail.com (Z. Ul-Haq).

Several inhibitors of p38 MAP kinases have been reported that effectively reduce cytokine levels in biological assays as well as in animal models [26–28]. Moreover, first generation p38 MAP kinase inhibitors have been dissatisfied due to their poor toxicity profiles [29]. These compounds possessing two heterocyclic moieties; pyridine and imidazole that acts as favorable ligands for heme iron (ferric) of cytochrome P450 [30]. Several other combinations were designed by replacing imidazole rings [31–33] with other suitable heterocycles, and sterically demanding substituents were introduced at the imidazole N1 [34]. Enhanced cell-based activity with better aqueous solubility was observed having poor oral bioavailability unless imidazole was methylated on nitrogen. Cytochrome P450 system inhibition studied by Laufer et al., provided compounds that have inhibition profiles against more than one system but contradictory results were obtained with the biological evaluations of these compounds [35]. Furthermore, selectivity screen with 119 kinases [36] and an updated selectivity screen with 317 kinases [37] showed that many other kinases are also inhibited by pyridinyl and pyrimidinyl imidazole inhibitors.

Still a structural feature has to be searched out that compromise with safe drug profile, along with potency and selectivity. Structural information reveals that the kinase hinge region of p38α MAP kinase is predominantly involved in hydrogen bonding interactions to some inhibitors with its backbone NH group of Met109 and Gly110. Another unique feature of such inhibitors is their potential for inducing a flipped conformation of the peptide bond connecting Met109 and Gly110 [38–41]. It has been long discussed that this feature could be used to gain selectivity over other kinases that lack glycine residue at the same position. In addition to the catalytically active conformations, the DFG-out arrangement is considered as one of the frequently encountered inactive kinase conformations [42,43]. The conserved DFG motif at the start of the activation loop is drawn into the ATP binding site and out, producing a new pocket that is difficult to appear in the active kinase conformation. However, access to this pocket is only made possible when allosteric inhibitors causes conformational changes in the apo form. The side chain of Phe169 (a gatekeeper residue) in the DFG-in conformation moves to a location that is 10 Å away, thus exposing a vacant hydrophobic grove that sterically impede with ATP binding site in the DFG-out conformation. This permits a vacant hydrophobic pocket that could be filled by the hydrophobic groups in the inhibitors. The existence of a dynamic equilibrium that lies between the DFG-in and DFG-out conformation in its apo and complex form has been first studied on the basis of the NMR results [44]. Besides NMR, Fremberg-Kesner and Elcock [45] reported the dynamic behavior of DFG loop by applying a high temperature (HT) MD simulation to fasten the DFG-in to DFG-out transition, coalesced with a docking protocol to analyze the different conformations of ligands. Binding of inhibitors to such sites entitled as allosteric inhibition [46–48]. A limited number of kinases adopt the DFG-out conformation and targeting such conformational states lead to better kinase selectivity.

Recently, a series of highly potent, selective, orally active, metabolically stable, and efficient in both acute and chronic animal model of inflammation, *N*-benzyl pyridinone derivatives has been reported as inhibitors of p38α MAP kinase [49]. Previously, a few 3D-QSAR studies have been published regarding the p38α MAP kinase inhibitors [50–54]. Our research group has also successfully reported several 3D-QSAR studies [55–58]. In this paper, we have unified the strengths of molecular docking and 3D-QSAR methods for the development of predictive models in an automated unbiased manner acknowledged as structure-based 3D-QSAR protocol. Instead of only relying information from the ligand molecules, docked poses are used to obtain the rational molecular alignment for developing 3D-QSAR models as docking also incorporates protein information during the generation of

each pose. After considering the overall good performance of 3D-QSAR [58], detailed molecular interactions were analyzed on the basis of MD simulation results. The major objective of this study apart from predicting the good ability for the whole series of *N*-benzyl pyridinone inhibitors is to highlight the selectivity differences triggered by the binding of allosteric inhibitors.

2. Methods

2.1. Data set and biological activities

For current 3D-QSAR studies, a data set of 40 *N*-benzyl pyridinone derivatives as p38α MAP kinase inhibitors was selected from the literature [49]. All compounds were associated with biological activities (IC_{50} values) ranging from 72 to 0.022 μM. IC_{50} values of the data set were converted into pIC_{50} by taking their inverse logarithms ($-\log IC_{50}$) and used as a dependent variable for further investigation. Thirty two out of 40 compounds were randomly selected as a training set for CoMFA and CoMSIA model construction while the remaining 8 compounds were used as a test set for the validation of constructed models. From Fig. 1, it is cleared that training and test set compounds were divided by considering both the distribution of biological data and structural diversity.

2.2. Computational details

2.2.1. Construction of 3D molecular structures

3D X-ray crystal structure of *Homo sapiens* p38α MAP kinase with 1-benzyl-4-(benzyloxy)-3-bromopyridin-2(1H)-one (SC-25028; **1**) inhibitor was retrieved from PDB (PBD ID: 3HP2) [49] to obtain the scaffold of **1**. The same scaffold was then utilized for designing *N*-substituted pyridinone analogues by the sketch module of SYBYL 7.3 [59]. First, the structure of **1** was assigned with Gasteiger-Marsili partial atomic charges [60], and then minimized using standard tripos force field [61] with distance dependent dielectric function by Powell method [62] until convergence criterion value of 0.05 kcal/mol Å was reached. Second, the remaining structures were constructed by similar approach employing **1** as a template and changing the required groups (R, Ar and Ar′). Each structure was then charged and minimized in the same manner. All protonated ligand files in .mol2 format with appropriately ionized polar groups were saved.
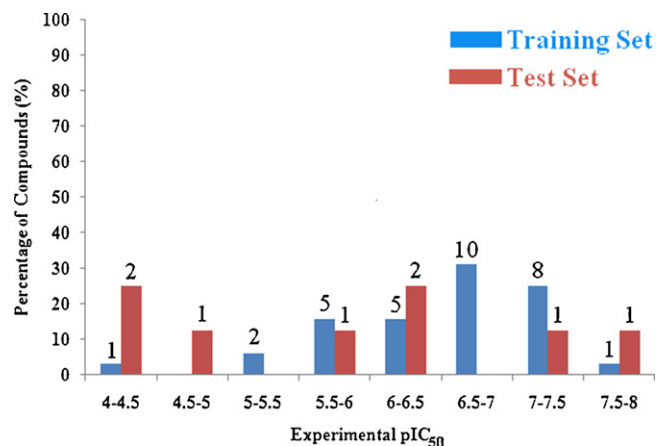

Fig. 1. Bar graph shows the experimental inhibitory activities for training and test set compounds. The number of compound(s) in each interval is indicated above the column.

2.2.2. Preparation of protein structure

Compound **1** and water molecules were removed from 3HP2. Missing residues were built and hydrogen atoms were added subsequently by SYBYL. In order to prevent from steric hindrance as caused by the addition of missing residues and hydrogen atoms, staged sub-minimization of protein was carried out by Powell method [62] employing 5000 steps of steepest descent and conjugate gradient each in Tripos force field [61]. A distance dependent dielectric constant of 1.0 R and a non-bonded atom cut off of 8.0 Å was used.

2.2.3. Molecular docking

To determine the most probable binding conformations of the whole data set, GOLD software (3.0) [63] has been used. The GoldScore fitness function incorporated with GOLD consists of four components: protein–ligand hydrogen bond energy, protein–ligand van der Waals (vdw) energy, ligand internal vdw energy and ligand torsional strain energy. GOLD atom-type checking was turned on for both ligand and protein atoms. An active site of 10 Å was chosen around **1** with centroid of $X = 35.3633$, $Y = 38.0561$, and $Z = 22.1456$. The default genetic algorithm parameters along with the annealing settings were used. Each molecule was docked with early termination if the top three poses were within 1.5 Å root mean square deviation (RMSD). In each case only one conformation was selected on the basis of GoldScore fitness function, in addition to visual inspection.

2.2.3.1. Re-docking of co-crystallized ligand.
Prior to docking, a protocol was established by the reproduction of X-ray complex. For this purpose, reference compound **1** was re-docked into the active site of p38α MAP kinase. The fitness evaluation of each re-docked pose was scrutinized by considering the RMSD values. The selected re-docked pose was further examined by its interactions with the target protein, confirming the efficiency of docking algorithm and scoring function by comparing with the bound conformation of **1**.

2.2.4. CoMFA and CoMSIA modeling

For CoMFA [64] and CoMSIA [65,66] studies, the position of a molecule is the most important factor since the descriptors are calculated on the basis of coordinates of atoms. The most favorable binding conformations obtained for each compound were aligned within active site of the protein. The partial least square (PLS) [67] method was used for all the 3D-QSAR analysis. Quality of the models was controlled by their cross-validated correlation coefficient (q_{cv}^2) and test set prediction (r_{pred}^2) values.

2.2.4.1. CoMFA.
CoMFA comprises of two fields namely, steric [Lennard–Jones (6–12 interactions)] interaction field and Columbic electrostatic potentials ($1/r$). These two field's energies were generated by placing the molecular alignment of all the *N*-benzyl pyridinone derivatives in a 3D cubic lattice with a grid step size of 2 Å. As a probe atom, sp³-hybridized carbon atom of +1 charge with radius of 1.52 Å was used at each intersection. Fields were calculated beyond the volumes for all investigated molecules in each direction (*x*, *y* and *z* coordinates). A distance dependent dielectric constant of 1.0 R was used using standard Tripos force field. In order to avoid steric and electrostatic energies domination, a cut off value of 30 kcal/mol scaled by CoMFA-STD method was set so that energies will not exceed to the larger values.

2.2.4.2. CoMSIA.
CoMSIA can reduce some inherent deficiencies that arise from the fields of Lennard–Jones and Columbic potentials calculated in CoMFA. In CoMSIA, five physicochemical properties (steric, electrostatic, hydrophobic, and hydrogen bond donor and acceptor) were evaluated. Moreover, a distance dependent of

Gaussian-type functional form instead of the traditional CoMFA potentials have been used between the grid points with default value of 0.3 for the attenuation factor, α for each compound. CoMSIA has better ability to visualize and interpret the obtained correlations in terms of field contributions. Similar to that of CoMFA, the molecular alignment was placed in 3D grid (2 Å spacing). Singularities were avoided at atomic positions in CoMSIA fields because assumption has been made for Gaussian-type distance dependence of the physicochemical properties; hence no arbitrary cutoffs were requisite. To derive fields of CoMSIA, an sp³-hybridized carbon atom was used as a probe atom with radius 1.52 Å and +1 charge with hydrophobicity of +1 (atom based parameters [68]), steric (by the third power of atomic radii), electrostatic (derived from partial atomic charges), and hydrogen bond donor and acceptor fields.

2.2.4.3. Regression analysis by PLS method.
A special multivariate statistical technique of PLS regression analysis implemented in SYBYL was utilized to obtain correlation between the descriptors derived by CoMFA and CoMSIA modeling studies while the actual biological activities (pIC$_{50}$) values were included in a molecular spreadsheet that were used as target dependent variables. Initially, cross-validation was performed using the leave-one-out (LOO) method [64,69] to minimize the tendency of over fitting the data, to check the predictivity of the derived model, and to determine the optimum number of components (ONC) with minimum standard error of prediction (SEP). The LOO method calculates as many models as there are data points (molecules) in the data set. In LOO method, one molecule, in turn, is removed from the data set and its activity is predicted using the model derived from rest of the data set. The minimum sigma as column filtering was assigned to 2.0 kcal/mol. This is necessary to accelerate the regression analysis and to reduce the signal-to-noise ratio by omitting the lattice points whose energy variations were below the adjusted threshold value. The q_{cv}^2 and SEP were calculated by the following equation:

$$q_{cv}^2 = 1 - \frac{\sum (Y_{obs} - Y_{pred})^2}{\sum (Y_{obs} - Y_{mean})^2} \tag{1}$$

$$\text{SEP} = \sqrt{\sum \frac{(Y_{obs} - Y_{pred})^2}{N}} \tag{2}$$

where Y_{obs} = experimental value, Y_{pred} = predicted value, Y_{mean} = average value and N = number of objects (molecules).

Final analyses were performed to calculate the non cross-validated correlation coefficient, r_{ncv}^2, using ONC obtained from the cross-validation procedure and their standard errors of estimate (SEE). The CoMFA and CoMSIA results were interpreted graphically by the contribution maps using the field type "PLSstdev × PLScoeff". To validate the CoMFA and CoMSIA derived models, the predictive ability r_{pred}^2 was determined for the test set molecules.

2.2.5. Molecular dynamics (MD) simulation study

The explicit solvent MD simulation studies were conducted for **12f**, **7a** and **8a** to observe the behavioral effects of inhibitors coupled with the changes in activity and effects on protein active site. Hydrogen atoms were added to the complexed systems using the internal coordinates of the AMBER all-atom database via XLeaP module of AMBER 10 [70]. The molecular mechanics (MM) parameters for these inhibitors (atom types and atomic charges) were assigned with the antechamber [71,72] module of AMBER 10. In particular, the inhibitors were assigned with generalized AMBER force field (GAFF) [71,72] atom types while AM1-BCC atomic charges were calculated with DivCon program on AMBER 10. Missing force-field parameters were assigned with the parmcheck utility. All calculations in this study were performed with AMBER 10 suite of programs and the ff03 [72] force field for the protein.

2.2.5.1. Structures generated with periodic boundary MD. Each protein–inhibitor complex was solvated in a rectangular box of TIP3P water molecules extending 8 Å outside the protein on each direction (Table 1). Ionizable residues were assigned correct protonation states that correspond to pH 7.0. The long-range electrostatic calculations were treated with the Particle Mesh Ewald (PME) summation [73] method. During simulation we used a residue-based cutoff of 9 Å to truncate non-bonded interactions, a time step of 2 fs for the integration of Newton's equation, and a constraint of bond lengths involving hydrogen atoms using the SHAKE [74] algorithm. The non-bonded pair list was updated after every 0.5 fs. The solvated protein–inhibitor complex systems were subjected to comprehensive energy minimization prior MD simulation. For this purpose, first restrain minimization of water molecules was done while frozen the solute (2500 steps using the steepest descent algorithm followed by 2500 steps of conjugate gradient minimizations of the whole system). During restrain minimization, the force of harmonic constraint was kept constant (25 kcal/mol Å^2) for water molecules, but for unrestrained minimization after every 500 steps force on counter ions was subjected to change (that was gradually decreased from 25 kcal/mol Å^2 to 5 kcal/mol Å^2 per 500 steps). This step was done to remove steric conflicts between protein–inhibitor complex, counter ions and water molecules, and to relax the entire system. Equilibration was performed by heating all systems at 300 K as follows: firstly, 65 ps equilibration at constant volume with 1 kcal/mol Å^2 restraint on the protein and inhibitors were performed in order to equilibrate the temperature from 0 to 300 K (with 100 K increments at 10 ps intervals) without undesirable drifts of structures that maintained for 35 ps. This state was regarded as the initial state. From this and onwards, equilibrium was re-continued under constant pressure conditions (1 atm) for 65 ps followed by 60 ps unrestrained MD with reduced restraints. This equilibration phase was not integrated for any subsequent analysis. After heating and equilibration to assess free energy convergence, 50 consecutive production MD that run the entire length of 100 ps each were performed, and coordinates were extracted after every 5 ps resulted in a hundred snapshots collected for each run, and a total of 5000 snapshots collected for each simulated system. Constant temperature (298 K) and constant pressure (1 atm) were controlled by the Berendsen coupling algorithm [75] with a time constant for heat-bath coupling of 0.2 ps. Mass-weighted RMSD analysis was performed using the PTRAJ module of AMBER 10 relative to the initial crystal structure. All trajectory plots were analyzed at a time interval of 1.0. Resulting trajectories were further examined by VMD (version – 1.8.6) [76] and CHIMERA (version – 1) [77] including phi–psi angles, interatomic distances, etc. Docking and 3D-QSAR studies were performed on a single Intel® Xeon® Quad™ core processor running under Linux OS (openSuSE 11.0). The MD simulation studies were calculated using the MPI SANDER module of AMBER installed on cluster computing facility at PCMD, ICCBS, University of Karachi, consisting of 10 nodes.

3. Results and discussion

3.1. Molecular docking analysis

3.1.1. Validation of docking protocol

Generally, the performance of docking software is judged from the resemblance of docked pose to the corresponding co-crystallized ligand. The available X-ray crystal structure of p38α MAP kinase in complex with **1** was undertaken to validate the docking reliability. All GoldScore fitness functions along with their RSMD values are showed in supplementary data (see Table S1 of Supplementary data). Eventually, all the re-docked
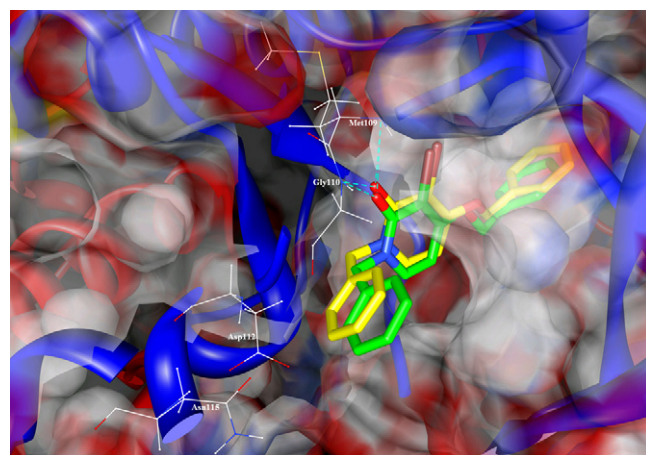

Fig. 2. Superposition of the selected re-docked pose (in yellow stick) to the crystal SC-25028 (**1**) (in green stick) at the active site of p38α MAP kinase. Met109, Gly110, Asp112 and Asn115 are shown as wire models with whole protein as surface electrostatic representation. Hydrogen bonding interactions are indicated as cyan dotted lines.

solutions reside almost at the same coordinating position as the co-crystallized ligand. The RMSD value between the selected re-docked pose of **1** against its bound conformation is 0.48 Å (Fig. 2). This indicates that the GOLD protocol and the GOLD parameters could be extended to search the binding conformations for other p38α MAP kinase inhibitors accordingly. The carbonyl oxygen atom (O1) of *N*-benzyl ring of co-crystallized ligand has two backbone hydrogen bonding interactions with NH of Met109 (3.21 Å) and Gly110 (3.01 Å). The selected re-docked pose of **1** also retains the same two key hydrogen bonding interactions (O1···HN-Met109 is 3.28 Å and O1···HN-Gly110 is 3.37 Å), suggesting a high reliability of GOLD docking method for structure-based 3D-QSAR that acts as a probe for protein–ligand interactions.

3.1.2. Docking results of p38α MAP kinase inhibitors

p38α MAP kinase has two characteristic domains separated by a deep channel where possible substrate might bind. One of the domain is relatively small, the N-terminal lobe, while the other is large, the C-terminal lobe. In between these two lobes, there is a highly conserved catalytic cleft where ATP binds. The two N and C lobes are connected by a hinge region where Met109 (a linker) is present [78]. N-terminal lobe mainly contains glycine residues known as glycine-rich loop, or simply as G-loop. This G-loop is highly flexible and capable of attaining different conformations, therefore, a backbone flip of Gly110 is observed for **1** because it forms a dual hydrogen bond with Met109 and Gly110 [49].

The interactions of different conformations for each inhibitor within the binding site were carefully inspected; moreover support from the GoldScore fitness function enabled us to select the most suitable conformation. One of the GOLD conformation of **12f** (GoldScore = 69.54) has carbonyl oxygen atom (O1) of *N*-benzyl ring that forms hydrogen bonding interaction with the backbone NH of Met109 (2.87 Å). The same oxygen atom of **12f** interacts with the NH of Gly110 (2.88 Å) (see Fig. S1a of Supplementary data). This occupancy pattern of *N*-benzyl pyridinone scaffold mimics the incoming adenine group of ATP molecule. The 2,4-difluorobenzyloxy moiety occupies the hydrophobic region I surrounded mostly by Leu residues (75, 86, 104 and 108), Ile84 and Thr106. Likewise, *N*-substituted *para*-carboxamide Ar′ moiety resides in the hydrophobic pocket II occupied by Val30, 38, Ala111 and Leu171. Furthermore, lipophilic interactions by *para*- and *ortho*-substituted fluorine atoms of benzyloxy group with the Cβ atoms of Leu104 (2.66 Å) and Ala51 (3.27 Å) render this compound

Table 1
The atomic composition of different solvated systems.

System	Total no. of residues	Total no. of residues atoms/including ligand atoms	Total no. of water molecules	Total no. of water atoms	Added counter ions	Total atoms	Box dimensions (Å³)
p38α_12f	341	5512/5558	10,998	31,947	7	37,512	90.266 × 76.664 × 68.898
p38α_7a	341	5512/5551	10,641	31,923	7	37,481	90.265 × 76.665 × 68.899
p38α_8a	341	5512/5555	10,640	31,920	7	37,482	90.264 × 76.665 × 68.889

more potent. Hence, it can be observed that **12f** retains key hydrogen bonding interactions and has similar binding mode to the co-crystallized ligand. The corresponding conformation of compound **12f** was selected as the most appropriate binding conformation. Thus, the most favorable docking conformation for each inhibitor was selected having similar binding pose as **12f** with high GoldScore fitness functions. Table 2 represents the GoldScore fitness functions of selected conformations.

If we compare interactions of **12f** with **7a**, the two key hydrogen bonding interactions were weak as compared to **12f** that is O1···HN-Met109 is 3.14 Å and O1···HN-Gly110 is 3.17 Å (see Fig. S1b of Supplementary data). The least active compound **8a** forms O1···HN-Met109 and O1···HN-Gly110 hydrogen bonding interactions at distances of 3.29 Å and 3.19 Å, respectively (see Fig. S1c of Supplementary data). The scores for hydrogen bonding interactions as output by LigX [79] clearly demonstrate that the decrease in activity is closely associated with the decrease in hydrogen bonding scores. It is also noteworthy that absence of any halogen isostere completely changes the binding pose of **8a** influencing the importance of electrostatic moiety in *N*-benzyl pyridinone inhibitors. Fig. 3 highlights the alignment of selected binding conformations of **12f** (the most active compound; 0.022 μM), **7a** (associated with intermediate activity; 0.9 μM), and **8a** (the least active compound; 72 μM) with the co-crystallized ligand **1**. The global alignment of all molecules in the series have one major difference in their orientation which mostly accounted for their SAR activity that is the phenolic group (Ar′) attached to the *N*-benzyl pyridinone ring (Fig. 4). CoMFA and CoMSIA studies elaborate more on this aspect.

3.2. CoMFA and CoMSIA statistical results

CoMFA and CoMSIA techniques were used to develop 3D-QSAR models for *N*-benzyl pyridinone inhibitors with p38α MAP kinase by selecting the best conformations for each inhibitor obtained
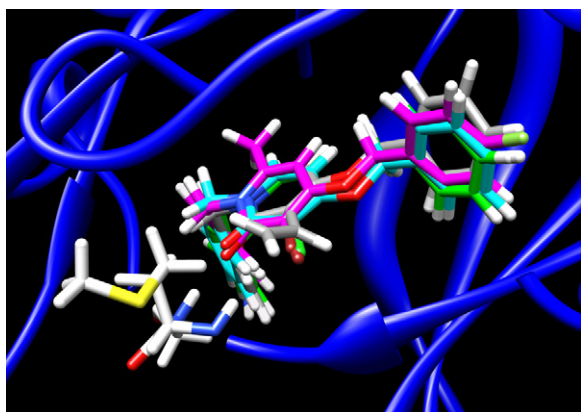

Fig. 4. Superimposition of all p38α MAP kinase inhibitors included in the training set. O is shown in red, C in silver, H in cyan, N in blue and halogens in green. All molecules are aligned onto the docked conformation of **12f**. Note the position of different substituents at Ar′ that accounts for SAR in the protein active site. (For interpretation of the references to color in this figure legend, the reader is referred to the web version of the article.)

from the docking results. Final models were selected according to the statistical parameters, $q_{cv}^2 \geq 0.5$, $r_{ncv}^2 \approx 1$, and the standard error of estimation (SEE). Later, the predictivity potential of the model was evaluated by randomly selected test set compounds.

CoMFA PLS statistical results are listed in Table 3. The optimal components that assign the best q_{cv}^2 value were used to produce r_{ncv}^2. The leave-one-out PLS analysis proposed good internal steadiness of the model. The contour map includes 47.20% of steric field descriptor whereas the proportion of electrostatic descriptor accounted for 52.80% indicating relatively higher influence of the electrostatic field than the steric field.

Table 4 shows a combinations of 20 different possible CoM-SIA field. Most of the CoMSIA models including electrostatic field showed high q_{cv}^2 values correlating the importance of electrostatic factor for *N*-benzyl pyridinone inhibitors as illustrated in CoMFA. CoMSIA model no. 3, 4, 8, and 10 has q_{cv}^2 values less than 0.5 that is 0.24, 0.49, 0.12, and 0.33, respectively. All these combinations have no electrostatic fields. However, CoMSIA model no. 2, 9, and 13 are also devoid of electrostatic field but still they have q_{cv}^2 greater than 0.5 that are 0.63, 0.56, and 0.58, respectively. Contributions due to the presence of different fields especially hydrophobic exhibit q_{cv}^2 values within the acceptable range. CoMSIA model no. 20 with five fields gave the best statistical result with q_{cv}^2 value of 0.68. The model was supported by 8.50% steric, 38.20% electrostatic, 16.30% hydrophobic, 19.0% hydrogen bond donor, and 18.0% hydrogen bond acceptor contributions of total variance with *F* value of 76.67.

Although, CoMSIA model nos. 11 and 12 were much simpler having few descriptors with higher q_{cv}^2 values (0.69 for both models) when compared to CoMSIA model no. 20 but the significant contributions by hydrogen bond acceptor and hydrogen bond donor fields of the latter model were indispensible. Moreover, if SEP value that points toward the over fitting of data decreases less than 5% due to the addition of any variable or descriptor, the simpler model is more preferable as it contains most of the information with fewer variables. If more variables are added, more noise is added to the model introducing redundant information. In our case, CoMSIA model nos. 11, 12 and 20 have the same SEP values (that is 0.45) indicative of the fact that the increase of variable did not lead the data to be over

Fig. 3. Alignment of the selected bioactive conformations of **12f**, **7a** and **8a** with the co-crystallized SC-25028 (**1**). **12f** (magenta), **7a** (cyan), **8a** (dark grey) and **1** (green) are shown as sticks. Met109 and Gly110 are also represented as stick models. Ile84-Leu86 is omitted for the sake of clarity. (For interpretation of the references to color in this figure legend, the reader is referred to the web version of the article.)
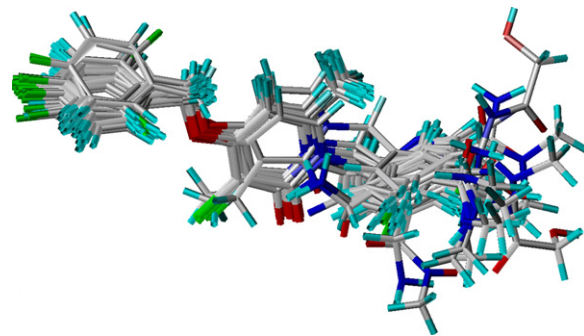
Table 2
Experimental biological activity and GoldScore fitness function for the training set and test set compounds. .

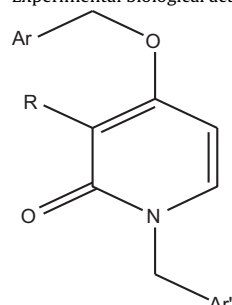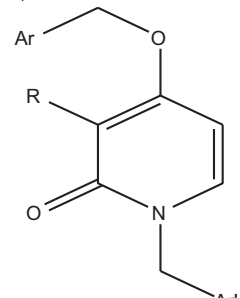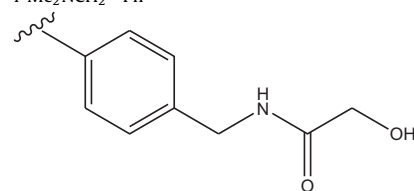| Compounds	R	Ar	Ar′	IC$_{50}$ (µM)	GoldScore fitness function
1[a]	Br	Ph	Ph	0.68	69.87
7a	Cl	Ph	Ph	0.9	68.49
7b[a]	I	Ph	Ph	3.1	71.44
7c	H	Ph	Ph	43	64.75
7d	Br	4-Cl—Ph	4-F—Ph	1.9	68.28
7e	Br	4-F—Ph	3-F—Ph	0.62	69.36
7f	Br	2,4-DiF—Ph	3-F—Ph	0.13	68.96
8a[a]	CH=CH$_2$	Ph	Ph	72	66.25
8b	Et	Ph	Ph	6.1	65.16
8c	Me	Ph	Ph	5.3	66.13
8d[a]	CF$_3$	Ph	3-F—Ph	50	66.14
8e[a]	CN	2,4-DiF—Ph	3-F-Ph	9.9	68.64

Compounds	R	Ar	Ar′	IC$_{50}$ (µM)	GoldScore fitness function
12a	Br	2,4-DiF—Ph	2-CN—Ph	1.2	69.30
12b	Br	2,4-DiF—Ph	3-CN—Ph	0.11	71.70
12c	Br	2,4-DiF—Ph	4-CN—Ph	0.19	70.85
12d	Br	2,4-DiF—Ph	2-NH$_2$C(=O)—Ph	2.67	65.48
12e	Br	2,4-DiF—Ph	3-NH$_2$C(=O)—Ph	0.27	69.16
12f	Br	2,4-DiF—Ph	4-NH$_2$C(=O)—Ph	0.022	69.54
12g	Br	2,4-DiF—Ph	3-NMe$_2$C(=O)—Ph	0.25	66.74
12h	Br	2,4-DiF—Ph	4-NMe$_2$C(=O)—Ph	0.066	68.25
12i	Cl	2,4-DiF—Ph	4-NMe$_2$C(=O)—Ph	0.079	67.96
12j	Br	2,4-DiF—Ph	3-NMeHC(=O)—Ph	0.2	69.31
12k[a]	Br	2,4-DiF—Ph	4-NMeHC(=O)—Ph	0.025	70.78
12l	Br	4-F—Ph	2-Pyridine	1	68.24
12m	Br	4-F—Ph	3-Pyridine	0.38	67.33
12n[a]	Br	4-F—Ph	4-Pyridine	0.39	67.51
12o	Br	2,4-DiF—Ph	3-Pyridine	0.15	67.61
12p	Br	2,4-DiF—Ph	4-Pyridine	0.21	67.52
12q	Br	2,4-DiF—Ph	2-(5-Me-pyrazine)	0.45	67.33
12r	Br	2,4-DiF—Ph	2-(5-HOCH$_2$-pyrazine)	0.45	67.90
12s	Br	2,4-DiF—Ph	5-(2-Me-pyrimidine)	0.18	67.93
15	Br	2,4-DiF—Ph	2-H$_2$NCH$_2$—Ph	1.26	71.93
16	Br	2,4-DiF—Ph	3-H$_2$NCH$_2$—Ph	0.065	70.73
17	Br	2,4-DiF—Ph	4-H$_2$NCH$_2$—Ph	0.12	71.09
18	Br	2,4-DiF—Ph	3-Me$_2$NCH$_2$—Ph	0.063	65.76
19	Br	2,4-DiF—Ph	4-Me$_2$NCH$_2$—Ph	0.059	73.51
20	Br	2,4-DiF—Ph		0.046	67.35

Table 2 (*Continued*)

Compounds	R	Ar	Ar′		IC$_{50}$ (μM)	GoldScore fitness function
21	Cl	2,4-DiF—Ph			0.055	76.24
22[a]	Br	2,4-DiF—Ph			0.049	75.69
23	Br	2,4-DiF—Ph			0.05	71.81

[a] Test set compound.

fitted. Therefore, we have chosen CoMSIA model no. 20 as the best one.

3.2.1. Validation of CoMFA and CoMSIA models

The ultimate characteristic property of 3D-QSAR technique is the validation of externally driven 3D-QSAR model by means of calculating quantitatively the activities of test set compounds. The 3D QSAR technique is validated externally by the prediction of test set compounds. Both models gave satisfactory results which are in good agreement with the actual substantiated by the CoMFA and CoMSIA r^2_{pred} values of 0.71 and 0.81, respectively. The actual versus predicted pIC$_{50}$ values of the training and test set compounds as derived by 3D-QSAR CoMFA and CoMSIA models are given in Table 5. The graphical representations of correlation between actual and predicted pIC$_{50}$ values for the two models are shown

Table 3
Summary of the CoMFA and CoMSIA PLS statistical results.[a]

PLS statistical parameters	CoMFA	CoMSIA
q^2_{cv} [b]	0.54	0.68
ONC[c]	6	5
r^2_{ncv} [d]	0.98	0.94
SEE[e]	0.11	0.20
SEP[f]	0.55	0.45
F-test ratio[g]	281.30	76.62
r^2_{pred} [h]	0.71	0.81
Field contributions (%)		
S	47.20	8.50
E	52.80	38.20
H	–	16.30
D	–	19.00
A	–	18.00

[a] *Abbreviations*: CoMFA and CoMSIA with different field contributions such as S (steric); E (electrostatic); H (hydrophobic); D (hydrogen-bond donor); A (hydrogen-bond acceptor).

[b] Cross-validated correlation coefficient after leave-one-out procedure.

[c] Optimum number of components.

[d] Conventional non cross-validated correlation coefficient.

[e] Standard error of estimate.

[f] Standard error of prediction.

[g] Ratio of r^2 explained to unexplained $= r^2/(1 - r^2)$.

[h] Predicted conventional non cross-validated correlation coefficient for the test set compounds.

in Fig. 5. Compounds **8a** and **8e**, are found to be outliers in both CoMFA and CoMSIA models with residual values of −1.91 and −1.10 for CoMFA and −1.29 and −1.26 for CoMSIA models, respectively. There are numerous reasons that might be responsible for

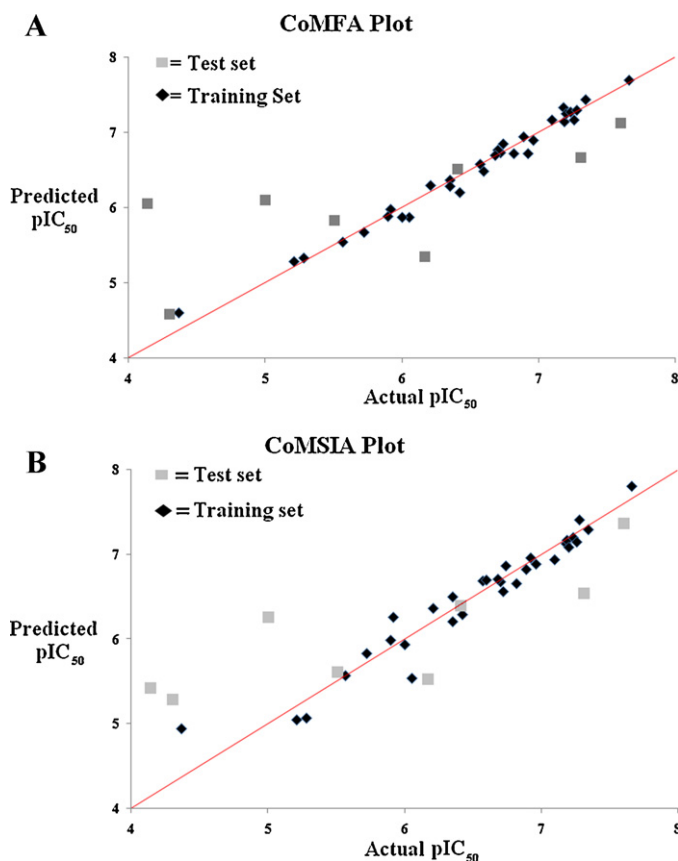**Fig. 5.** Experimental biological activities (actual pIC$_{50}$) values plotted versus the predicted values of bioactivity which were obtained from the selected models: (A) CoMFA; (B) CoMSIA. The triangles and squares refer to the training and test set, respectively while holding the trend line. (For interpretation of the references to color in this figure legend, the reader is referred to the web version of the article.)

outliers, for example, an incorrectly measured experimental value, a significant difference in the physiochemical properties, a different binding conformation, or structural uniqueness. Our results showed that due to distinct structure these outliers might act by a different mechanism or interacting with the receptor in a different mode. The potential drawbacks of the outlier is that it limits the described binding mode on the basis of few descriptors of our model, secondly it also indicates the possible failures of the model in experiments as the outlier misfits in the model or it may differ in interaction pattern at the binding site as compared to other compounds. The QSAR model (from the residual values of **8a** and **8e**) and MD simulation analysis indicates that these outliers showed a different interacting pattern with the receptor in different modes. The presence of unsubstituted phenyl rings as Ar and Ar′ and the absence of halogen substituent at the 2,4-difluorobenzyloxy group are possible reasons for outlier behavior.

3.3. Visual inspection and interpretation of CoMFA and CoMSIA contour maps

The level-dependent contouring of standard CoMFA-field contributions indicates those regions in space where the aligned molecules would favorably or unfavorably interact with the environment. The 3D-QSAR produced by CoMFA and CoMSIA with final r_{ncv}^2 PLS analysis was used to generate 3D contour maps using the field type equation coefficients (PLSstdev × PLScoeff), thus providing the visual interpretation of statistical analysis. 3D contour plots proposed further insights requisite to design novel molecules. Superimposition of 3D contour maps and p38α MAP kinase binding pocket was done to correlate binding pocket with contours. Usually the most active compound, that is **12f**, is rooted in the maps to demonstrate its affinity for different regions of contour maps.

3.3.1. CoMFA contour maps

Compound **12f** served as a reference molecule since it is the most active compound in the whole data set (IC$_{50}$ = 0.022 μM). The CoMFA steric and electrostatic fields are presented as contour plots in Fig. 6. The steric field is indicated by green (favored – 85%) and

Fig. 6. CoMFA StDev*Coeff steric and electrostatic contour maps based on reference compound, **12f** (ball and stick model). Increased binding affinity is correlated with: more bulk near green, less bulk near yellow in the steric map; more positive charge near blue, more negative charge near red in the electrostatic map. Crucial binding site amino acid residues of p38α MAP kinase are also shown (wire model). Some binding site atoms are colored green indicating their involvement in interactions with different inhibitors observed during literature survey [80]. (For interpretation of the references to color in this figure legend, the reader is referred to the web version of the article.)

yellow (disfavored – 15%) color contributions while electrostatic region comprises of blue (electropositive – 80%) and red (electronegative – 20%) color contributions. In the steric field of CoMFA contour maps, the favorable (green) region shows that the bulkier substitution will enhance the biological activity of the compound while the sterically disfavored (yellow) region indicates that the presence of bulky group is likely to decrease the activity. The electrostatic field as designated by blue and red contours depicts the position where positively charged and negatively charged moieties would be favorable, respectively.

3.3.1.1. CoMFA steric contour maps. Two sterically disfavored regions are present near the carboxamide phenolic ring system of **12f**. One steric disfavored region is located near the residues Asp112 and Asn115 while the other is present closed to the Leu167 and 171 shows that the presence of any bulkier group will not adjust properly in this small binding site. These contour maps are consistent with the experimental phenomenon in which substitutions at *ortho* position (**12d**) were not tolerated by *N*-benzyl pyridinone inhibitors. This further explains that the *para*-substituted carboxamide compound that is **12f**, **12h** and **12i** offered more potency than *meta*-substituted compounds (**12e**, **12g**, and **12j**). However, the activity of **12f** decreases when carboxamide group is replaced by dimethylcarboxamide group in compound **12h**. But both **12i** and **12h** are more active in rLPS model of inflammation than **12f**. The substituent dimethylamine present at *para* position of **19** is more active as compared to the compound **18** in which the same substituent is present at *meta* position. Although, compound **17** has *para*-substituted methylamine yet the presence of dimethylamine in **19** favors its interaction with Val38 and Leu141 further augmenting its potency. **16** and **19** when compared indicates better activity of **16** as compared to **17** and **18**, since **16** has *meta*-position with only methylamine substituent. *Ortho*-substituted methylamine at yellow isopleth further decreases the activity of **15**. Compounds **20**, **21** and **22** with OH-carboxamide moiety also have comparable potency than neutral carboxamide analogs. Substitution of cyanide group at *meta* position (**12b**) has more biological activity than *para*-substituted (**12c**) since nitrogen of cyanide group of **12b** engages itself into the hydrogen bonding interactions with Asp112 and Asn115. The cyanide group at *para* position of **12b** is sandwiched between the two sterically disfavored regions. It is interesting to note that the presence of dimethylcarboxamide at *para* position of **12h** has high bulkiness as compared to **12f** that correspond to low activity of **12h**. Substitution of methylcarboxamide at *meta* position in **12j** further decreases the activity due to the presence of steric bulk close to the methyl group of carboxamide.

The structure of molecules with different halogen isosters lead to the improvement of biological activities that fits in the binding site more appropriately than other groups depending upon their size. Two sterically favored regions are present near X substitution of the *N*-benzyl pyridinone ring (Fig. 6) suggested that the presence of bulky groups in these regions favor the kinase inhibitory activity and SAR also suggested the same as evidenced by more bulky bromine atom. The presence of bromine in **12f** is consistent with the favorable region of steric contour map as atomic radii of F < Cl < Br < I. The same effect is seen in compounds **7a** (X = Cl), **7c** (X = H), and **21** (X = Cl) that are less potent as compared to their bromine counterparts. Two other green isopleths are also sighted at *ortho* and *para* positions of 2,4-DiF—Ph ring of **12f**. This further explains the difference in the activity of **12l** and **12o**. **12l** has only fluorine atom at *para* position while **12o** has two fluorine atoms at *ortho* and *para* position augmenting the efficiency of developed CoMFA maps. **12m** and **12o** when compared showed that the activity is increased when fluorine atom is added at *ortho* position in **12o** besides with the *para* position. Similar SAR is also observed for **7e** and **7f**. However, if we compare **7e** and **7d** in which fluorine is
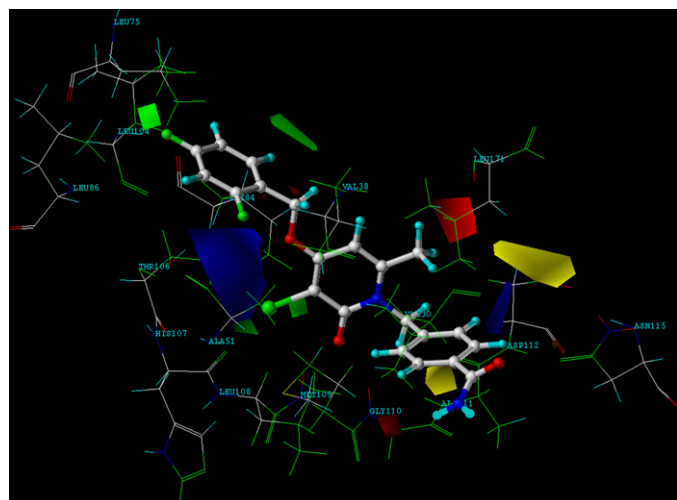
Table 4
Summary of results of different CoMSIA models.

Model no.	Field combinations	q_{cv}^2 [b]	r_{ncv}^2 [d]	ONC[c]	SEE[e]	SEP[f]	F ratio[g]	Field contributions[a]				
								S	E	H	D	A
1	S + E	0.57	0.85	3	0.30	0.51	52.95	13.10	86.90	–	–	–
2	S + H[i]	0.63	0.93	5	0.21	0.49	69.97	23.60	–	76.40	–	–
3	S + D[j]	0.24	0.62	4	0.49	0.69	10.86	34.60	–	–	65.40	–
4	S + A[j]	0.49	0.76	5	0.39	0.57	16.83	33.10	–	–	–	66.9
5	E + H	0.68	0.94	5	0.10	0.46	88.50	–	68.50	31.50	–	–
6	E + D	0.62	0.90	5	0.25	0.50	48.70	–	71.70	–	28.30	–
7	E + A	0.52	0.81	3	0.33	0.54	40.61	–	70.30	–	–	29.70
8	H + D[j]	0.12	0.71	3	0.42	0.73	22.46	–	–	45.10	54.90	–
9	H + A[i]	0.56	0.86	4	0.30	0.52	41.60	–	–	52.80	–	47.20
10	D + A[j]	0.33	0.62	6	0.50	0.67	6.83	–	–	–	35.90	64.10
11	S + E + H	0.69	0.95	5	0.18	0.45	104.20	8.80	61.60	29.70	–	–
12	E + H + D	0.69	0.94	5	0.20	0.45	81.48	–	56.50	20.10	23.30	–
13	H + D + A[i]	0.58	0.90	6	0.26	0.53	37.31	–	–	39.90	25.00	35.10
14	S + E + A	0.56	0.87	4	0.28	0.53	46.33	9.70	62.00	–	–	28.30
15	S + E + H + D	0.66	0.94	5	0.20	0.47	81.52	6.30	52.30	18.70	22.60	–
16	S + E + H + A	0.67	0.95	5	0.17	0.46	106.81	8.00	46.80	25.00	–	20.30
17	S + E + D + A	0.62	0.91	5	0.25	0.49	49.65	7.00	51.30	–	23.40	18.20
18	S + H + D + A	0.63	0.92	6	0.24	0.50	44.63	10.70	–	34.70	22.70	31.90
19	E + H + D + A	0.69	0.93	5	0.21	0.45	72.74	–	44.90	17.70	20.30	17.00
20[*]	**S + E + H + D + A**	**0.68**	**0.94**	**5**	**0.20**	**0.45**	**76.67**	**8.50**	**38.20**	**16.30**	**19.00**	**18.00**

[a] *Abbreviations*: CoMFA and CoMSIA with different field contributions such as S (steric); E (electrostatic); H (hydrophobic); D (hydrogen-bond donor); A (hydrogen-bond acceptor).
[b] Cross-validated correlation coefficient after leave-one-out procedure.
[c] Optimum number of components.
[d] Conventional non cross-validated correlation coefficient.
[e] Standard error of estimate.
[f] Standard error of prediction.
[g] Ratio of r^2 explained to unexplained $= r^2/(1 - r^2)$.
[h] Predicted conventional non cross-validated correlation coefficient for the test set compounds.
[i] Field combinations having q_{cv}^2 values greater than 0.5 in the absence of electrostatic field.
[j] Field combinations having q_{cv}^2 values less than 0.5.
[*] CoMSIA model no. 20 highlighted in **bold** is considered as best CoMSIA model.

replaced by chlorine atom at Ar of **7d**, but the activity decreases due to the presence of *para* fluorine in Ar′ of **7d** located close to the steric bulk disfavored region (Fig. 6). Methyl and ethyl substitutions at X of **8b** and **8c** further decrease the inhibitory effects due to their unfavorable bulk effects (see Figs. S2a and S2b of Supplementary data).

3.3.1.2. CoMFA electrostatic contour maps. The CoMFA electrostatic contour maps show the electronegative favorable region as red and positively charged favorable region as blue. The red contour near carboxamide phenolic ring of **12f** indicates that the presence of electronegative moiety might increase the biological activity of compounds. The pyridine-(**12l**, **12m**, **12n**, **12o** and **12p**), pyrazine-(**12q** and **12r**) and pyrimidine-(**12s**) substituted *N*-benzyl pyridinone p38α MAP kinase inhibitors as Ar′ reflects the consistency in activity due to the presence of electron withdrawing group of their ring nitrogen atom. 3-Pyridine is the most influential substituent in **12o** as the presence of favorable red contour at *meta* position improves the activity of **12o**. The comparison between compounds **12o** and **12s** showed that the 3-pyridine ring of **12o** is slightly more favorable than the 2-methylated pyrimidine ring. The presence of 3-pyridine in **12o** is further justified by the replacement of 4-pyridine in **12p** that is responsible for decrease in activity. Compounds that have *para* substituted fluoro phenyl group as Ar (**12l**, **12m** and **12n**) have low activity as compared to their difluoro substituted ring. Out of these, **12m** has higher activity due to the presence of 3-pyridine ring near the favored red contour map. However, **12s** has more potency than **12q** since N4 of pyrazine is located away from the favored red contour map. Additionally, the presence of methyl group at *meta* increases the activity of **12s**. Presence of *meta* substituted fluoro phenyl group in **7e** near the red electronegative favored region has increased the activity of the compound as compared to **7d** where *para* substituted fluoro phenyl group is

present. Two blue contours are found that complement the electropositive character of inhibitors. One blue isopleth is located at C3 of *N*-benzyl pyridinone ring of **12f** where Met109, Gly110, Asp 112 and Asn115 are displayed while the second is present nearby carboxamide phenol ring. Electropositive character at C3 would be favorable in the following manner (I > Br > Cl > F). The presence of bromine is more favorable than the compounds which contain Cl at this region so that the activity of bromine containing compound is greater than that of chlorine containing compounds (compare **12h** and **12i**, and **20** and **21**). It also supports the decreased activity of **8e** compound having CN group that does not show electropositive character.
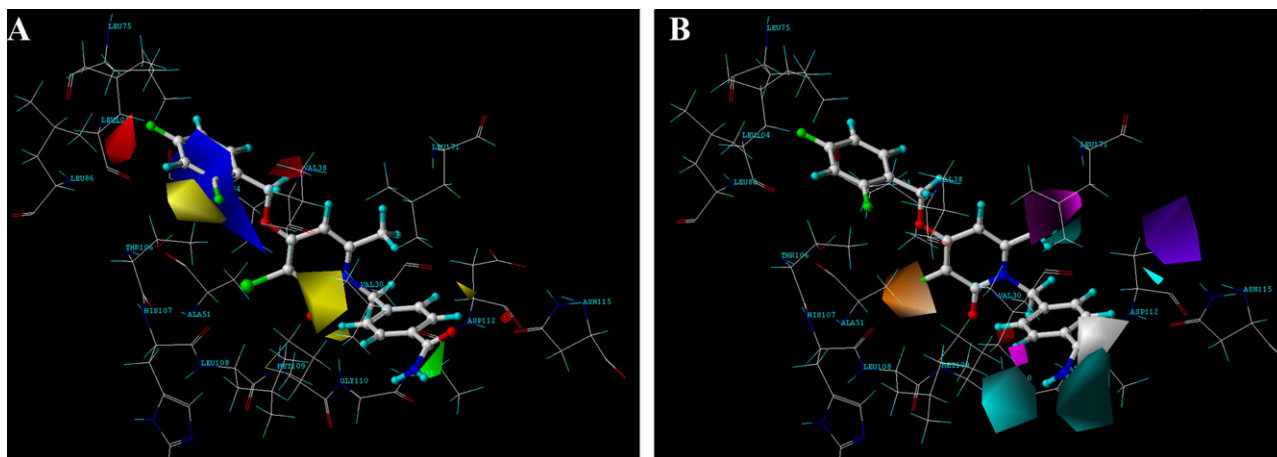
3.3.2. CoMSIA contour maps

The steric (favored – 95% and disfavored – 5%), and electrostatic (favored – 85% and disfavored – 15%) contour maps from the CoMSIA analysis are generally in accordance with the CoMFA maps (Fig. 7A and B). The steric favorable green and unfavorable yellow regions occupy the same position as in CoMFA. The negatively charged favorable region is also located very close to the CoMFA results. The contour maps of hydrophobic favored (orange – 85%) and disfavored (white – 15%) regions, hydrogen bond donor favored (cyan – 80%) and disfavored (purple – 20%) regions, and hydrogen bond acceptor favored (magenta – 90%) and disfavored (green-blue – 10%) regions were observed as the remaining CoMSIA fields.

3.3.2.1. CoMSIA steric and electrostatic contour maps. The CoMSIA steric and electrostatic contour maps are comparatively similar to the CoMFA contour plots of steric and electrostatic fields. The favored electronegative contour map of CoMSIA is positioned at *para* position of 2,4-DiF—Ph ring of **12f**. Favored electropositive blue region is passing through the center of the 2,4-DiF—Ph ring. As

Table 5
Actual verses predicted (CoMFA and CoMSIA) activities with residuals for p38α MAP kinase *N*-benzyl pyridinone inhibitors in the training set and test set compounds.

Compounds	Actual pIC$_{50}$	CoMFA predicted pIC$_{50}$	Residuals	CoMSIA predicted pIC$_{50}$	Residuals
1[a]	6.17	5.34	0.83	5.54	0.63
7a	6.05	5.88	0.17	5.55	0.50
7b[a]	5.51	5.83	−0.32	5.62	−0.10
7c	4.37	4.60	−0.23	4.94	−0.57
7d	5.72	5.67	0.05	5.83	−0.11
7e	6.21	6.30	−0.08	6.38	−0.16
7f	6.89	6.95	−0.06	6.83	0.06
8a[a,*]	4.14	6.05	−1.91	5.43	−1.29
8b	5.21	5.29	−0.08	5.06	0.15
8c	5.28	5.33	−0.05	5.08	0.20
8d[a]	4.30	4.58	−0.28	5.29	−0.99
8e[a,*]	5.00	6.10	−1.10	6.26	−1.26
12a	5.92	5.98	−0.06	6.27	−0.35
12b	6.96	6.90	0.06	6.89	0.07
12c	6.72	6.73	−0.01	6.57	0.15
12d	5.57	5.54	0.02	5.58	−0.01
12e	6.57	6.59	−0.01	6.69	−0.12
12f	7.66	7.70	−0.04	7.82	−0.15
12g	6.60	6.49	0.11	6.70	−0.10
12h	7.18	7.33	−0.15	7.13	0.05
12i	7.10	7.17	−0.07	6.94	0.16
12j	6.70	6.77	−0.07	6.69	0.02
12k[a]	7.60	7.12	0.48	7.37	0.23
12l	6.00	5.87	0.13	5.94	0.06
12m	6.42	6.21	0.21	6.30	0.12
12n[a]	6.41	6.51	−0.10	6.39	0.01
12o	6.82	6.72	0.09	6.66	0.16
12p	6.68	6.70	−0.02	6.71	−0.03
12q	6.35	6.37	−0.02	6.50	−0.15
12r	6.35	6.29	0.06	6.21	0.14
12s	6.74	6.85	−0.11	6.87	−0.13
15	5.90	5.88	0.02	6.00	−0.09
16	7.19	7.15	0.04	7.18	0.01
17	6.92	6.72	0.20	6.97	−0.05
18	7.20	7.23	−0.05	7.08	0.11
19	7.23	7.28	−0.05	7.20	0.03
20	7.34	7.43	−0.09	7.30	0.04
21	7.26	7.17	0.09	7.15	0.11
22[a]	7.31	6.67	0.64	6.54	0.77
23	7.28	7.30	−0.02	7.41	−0.13

[a] Test set compound.
[*] **8a** and **8e** are the two outliers.

Fig. 7. CoMSIA StDev*Coeff contour maps based on reference compound, **12f** (ball and stick model). (A) Steric and electrostatic contour maps and (B) hydrogen bond acceptor and hydrogen donor contour maps. Increased binding affinity is correlated with: more bulk near green, less bulk near yellow in the steric map; more positive charge near blue, more negative charge near red in the electrostatic map; more hydrophobic near orange, less hydrophobic near white in the hydrophobic map; more hydrogen bond donor near cyan, less hydrogen bond donor near purple in the hydrogen bond donor map; more hydrogen bond acceptor near magenta, and less hydrogen bond acceptor near green-blue in the hydrogen bond acceptor map. Crucial binding site amino acid residues of p38α MAP kinase are also shown (wire model). (For interpretation of the references to color in this figure legend, the reader is referred to the web version of the article.)

suggested by SAR, the presence of fluorine atom at *para* position of Ar group has improved activity in general because of the presence of red isopleth. The compound **7d** having chlorine at *para* position in Ar ring has less activity than **7e** since fluorine is replaced by chlorine atom while the activity of **7f** is further enhanced due to the presence of two fluorine substituents.

3.3.2.2. CoMSIA hydrophobic contour maps. The favored orange CoMSIA contour plots indicate that the presence of hydrophobic moiety would be beneficial for interactions with the active site region of buried Thr106 of p38α MAP kinase. This further explains the difference in the biological activities of **8c** (more active) and **8b** (less active). In **8c**, the methyl group is buried in the hydrophobic favored region while the ethyl group of **8b** is located away from the hydrophobic contour map. One white hydrophobic contour map is also observed. This is the region where Val30 and Leu171 are present so the substituent at this position should be less crowded.

3.3.2.3. CoMSIA hydrogen donor contour maps. Cyan-colored favorable hydrogen bond donor effect was observed by the presence of two contour plots near the NH_2 group of carboxamide substitution in **12f**. This pointed out the necessity of hydrogen bond donor group at this position, as this is the case shown by SAR of compounds. That may be the reason that why **12h** is less active than **12f**. Although **12h** has more steric bulk at its Ar′ *para* position yet the presence of two methyl groups decreases the activity. In contrast to this, the presence of cyanide group (a hydrogen bond acceptor group) at *para* position has low affinity as compared to *ortho* substituted CN group. **12o** is more potent than **12p** because **12o** has 3-pyridine having N as an acceptor group which is present away from the cyan region while **12p** has 4-pyridine in which N is slightly near to the cyan region, unfavorable for the activity of compound.

3.3.2.4. CoMSIA hydrogen acceptor contour maps. The favorable hydrogen bond acceptor magenta region is present near the C6 methylation of *N*-benzyl pyridinone ring. Another favorable isopleth is present near the *meta* position of Ar′ adjacent to the NH_2 group of carboxamide moiety. The *N*-benzyl group that has *meta* substituted CN ring (**12b**) has more activity than *ortho* (**12a**) and *para* (**12c**) substituted cyanide rings. Likewise, **16** and **22** have more potencies than their **17** and **21** counterparts since –CH_2NH_2 group and long chain hydroxyl carboxamide group are located at *meta* rather than at *para* position.

3.4. Structural analysis by MD simulation

MD simulation could be a significant tool for validating experimentally defined biological activities by searching a representation of the interaction network between an inhibitor and the protein. The structural intermediates which lead the protein to change its active site conformation were also investigated against their respective inhibitor.

3.4.1. Physical parameters of MD simulations

Fig. 8A shows mass-weighted RMSDs of all systems (only polypeptide backbone) calculated as a function of time indicating the stability of protein atoms during simulation. All systems are converged at a value less than 3 Å. The black curve of p38α_12f system shows that a plateau is formed approximately between 1500th and 7900th frame. This rise in **12f** could be augmented by a change in the conformation not observed in other systems. The other two systems, p38α_7a (red line) and p38α_8a (green line) almost has the same overlapping features that deviate apart at 9700th frame till the end of simulation run time.
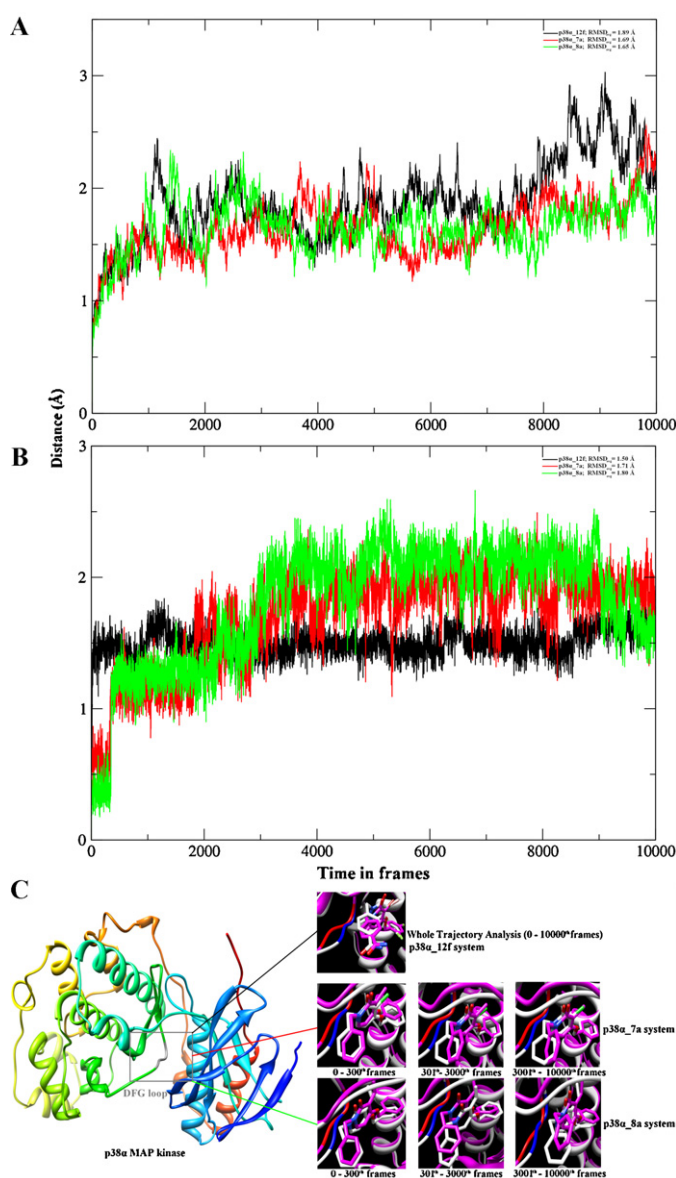

Fig. 8. Mass-weighted RMSD plots of (A) whole polypeptide backbone and (B) only DFG loop of all systems. The DFG loop conformation is displayed in (C) at different time intervals. The white ribbon (protein) along with the stick model (inhibitor) represents the starting structure superposed on the magenta ribbon (protein) along with the stick model (inhibitor) that shows the mass-weighted backbone RMS fit average structure within the particular time frame.

3.4.2. Structural changes in DFG loop

Fig. 8B shows mass-weighted RMSD plots belonging to the DFG loop of only protein atoms that allowed the explanation of dynamic behavior for each MD simulation. By analyzing the trend of RMSD plot, it is cleared that the p38α_12f system has the least RMSD$_{avg}$ value of 1.50 Å. However, the remaining two systems have substantial changes at the beginning (from 300th to 1900th frame) and at 3000th frame. Till this frame, RMSD value is increased from 0.62 Å to 1.76 Å for p38α_7a system (RMSD$_{avg}$ 1.32 Å – red line), and from 0.60 Å to 1.85 Å for p38α_8a system (RMSD$_{avg}$ 1.32 Å – green line). A plateau can be observed for p38α_7a system till the end but p38α_8a system shows further modification of the DFG loop conformation from higher values of oscillations to lower values of displacements.

Fig. 8C displays the calculated mass-weighted backbone RMS fit average structure at different time frames specifically

representing the variable DFG loop conformations. This removed the ambiguity of rotation and translational aspects. The DFG loop of p38α_12f complex is fairly maintained as DFG-out conformation. **7a** constrained the DFG loop as pseudo-DFG conformation while **8a** causes DFG-in conformation. This conformation of p38α_8a system causes the protein to be in the active kinase state, resulting the inhibitor less selective and least effective for the whole series.

3.4.2.1. Backbone and side chain movements in p38α MAP kinase by N-benzyl pyridinones. To enumerate changes in the DFG loop conformation, certain positions of atoms have been standardized for p38α MAP kinase. Two atoms, $C\alpha$ of Lys53 and Asn114, which lie on either side of the DFG loop, were chosen as reference points since their positions were found to be consistence in the whole range of p38 MAPK structures. Any confounding effects were also prevented from the $C\alpha$ atoms of these residues (less than 1 Å side chain movements). The distances between these two atoms to the C4 carbon atom of Phe169 provides a quantitative measure of variability to trace the changes in transition for DFG loop conformation, and the relative positioning of Phe169 side chain. Despite of Asp168 and Gly170, Phe169 residue was selected because of its bulk property. Shifting of this residue generates space that could potentially be filled with ligand atoms. The average Lys53–Phe169 distances (LysPhe$_{avg}$) for DFG-in and DFG-out conformations are 15.51 Å and 9.68 Å, respectively. If we compare the same values to our all simulated systems, than the DFG loop conformation maintained by **12f** is DFG-out, the most sensitive and unique conformation for the inhibition of p38α MAP kinase. The LysPhe distance is sustained at an average of 10.58 Å (see Fig. S3a of Supplementary data). Furthermore, the average Asn114–Phe169 distances (AsnPhe$_{avg}$) are 18.54 Å and 11.54 Å for the DFG-in and DFG-out conformations, respectively. **12f** also preserve this distance in favor of DFG-out conformation at an average distance of 14.16 Å (see Fig. S3b of Supplementary data). All these average distances are further supported by the backbone peptide flip of Met109. To quantify the backbone flip in the hinge region, the backbone ψ angle of Met109 (ψ_{109}) was used. Negative values of ψ_{109} indicate a flip in the backbone whereas positive values of ψ_{109} indicate that the backbone is not flipped. At the start of simulation run time for p38α_12f system, the peptidic NH group of Met109 remains in the flip form as indicated by the negative values of ψ_{109} angles. However, from 1250th to 4800th frame the ψ_{109} angle back and forth between positive and negative values showing conformational space of a polypeptide backbone. Such concerted fluctuations of ψ_{109} swing the amide bond connecting Met109 and Gly110. On the other hand, the O1 of **12f** forms two hydrogen bonds, one with the backbone NH of Met109 and the other with the polypeptide NH of Gly110. During the back and forth motion that completely reverses the orientations of the carbonyl and amino moieties from their apo conformations, **12f** is positioned further downstream, or **12f** might be slipped due to the space continuously provided by the repeatedly moving ψ_{109} by utilization its electrostatic atoms. Two fluorine and one bromine atom of **12f** causes the compound to be in the more vacant, and electronegative space (Lys53). After 4800th frame, the oscillations of ψ_{109} reverse back to the negative values completely with the re-formation of hydrogen bond between Gly110 and O1 of **12f** that broke during the ψ_{109} oscillations. Due to the presence of only one chlorine atom in **7a** and **8a**, no more pronounced effect is possible to be seen on the DFG loop conformation (Fig. 8C).

The hydrogen bonding interaction formed within p38α_7a system between O1···HN-Gly110 is broken at the start of simulation run time and lost till the end (Fig. 9A). An almost same phenomenon is occurred with p38α_8a system (at 1100th frame) but the hydrogen bond is formed once again around 8300th frame). Although protein provides a chance for **8a** to be displaced more into the allosteric binding site but due to the absence of any halogen
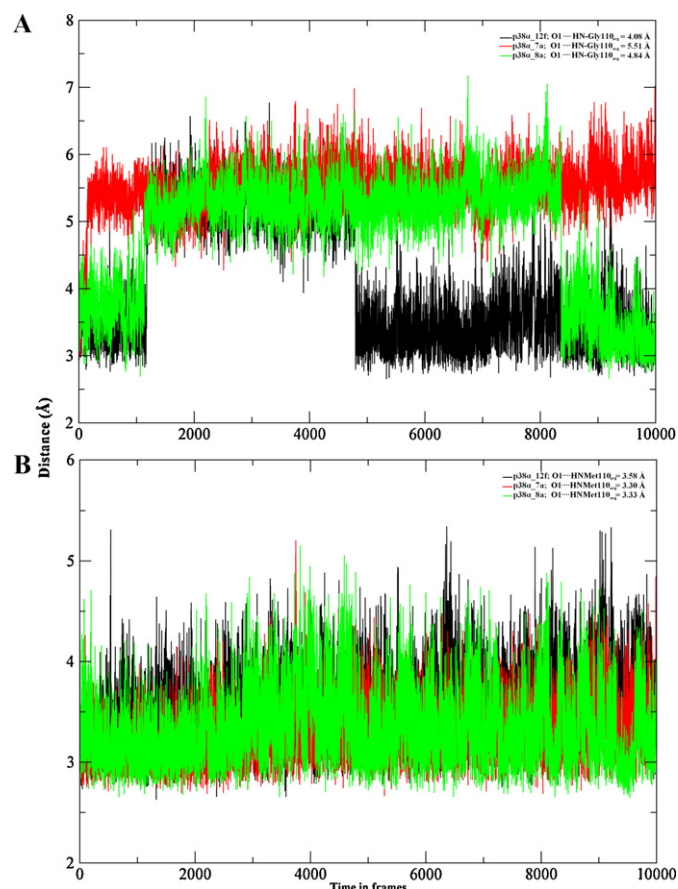

Fig. 9. Hydrogen bonding interactions: (A) O1···HN-Gly110 and (B) O1···HN-Met109 of all simulated systems along with their average values are shown. (For interpretation of the references to color in this figure legend, the reader is referred to the web version of the article.)

isostere, the re-association of hydrogen bonding interaction renders the DFG loop to be in the DFG-in conformation. The average values for hydrogen bonding interaction before (till 1100th frame; 3.74 Å) and after (8300th frame and onwards; 3.52 Å) re-association clearly indicates that although the interaction is weak but enough to keep DFG-in conformation. However, p38α_12f system keeps tracing the p38α_8a system but approximately at 4800th frame hydrogen bond is formed once again but much weaker than the p38α_8a system (from 4800th frame till onwards; 3.72 Å). This distance maintains a suitable balance between the DFG-out conformation and halogen isosteres of **12f**. The average O1···HN-Met109 hydrogen bonding distance of p38α_12f is also low as compared to other systems (Fig. 9B).

4. Conclusion

RA is characterized by chronic inflammation of multiple joints and marked destruction of cartilages and bones. In current study, a combined computational approach was utilized to gain insight into the structural basis and inhibition mechanism for a series of *N*-benzyl pyridinones as p38α MAP kinase inhibitors. We have employed the structure-based approach of 3D-QSAR by docking to explore the possible binding modes. The high quality of developed 3D-QSAR models is measured by a set of thorough criteria that showed their reliable predictive power and structure–activity correlation. Inherent molecular surface property mapping of 3D-QSAR helped us to highlight the cause of *N*-benzyl pyridinone selectivity for p38α MAP kinase. MD simulation study further supported the observation of conformational changes within p38α MAP kinase

as influenced by the inhibitors. All these explanations would be beneficial in designing more potent and selective inhibitors.

The difluorophenyl ring and bromine substitution on the benzyloxy ring is seemed to play a major role in the enhanced activity of compound **12f**. On comparison with the moderately (**7a**) and least active (**8a**) compounds, it is observed that the replacement of bromo substituent with chlorine, and the difloro substituted phenyl with unsubstituted phenyl moiety leads to reduce the inhibitory activity. It is also inferred that the presence of Gly110 adjacent to the linker Met109 residue (since only 9.2% of kinases expressed a glycine amino acid next to the linker region) might be accounted for better selectivity. The docking of the present data set utilized the same selectivity filter as dual hydrogen bonds to Met109 and Gly110 that requires an induced backbone flip of NH Met109. The need for both steric groups is well correlated with our 3D-QSAR models. It can be concluded that the carboxamide substitution at the *N*-benzyl group fulfils the need of hydrogen bond donor moieties as the region is mostly directed towards the solvent front. As discussed provisory, pyridine substitution leads to less potency but better bioavailability because the electron withdrawing effect of nitrogen blocks the oxidative cleavage of C—O and C—N bonds. Presence of red isopleths indicated the same charge effect that would be used for better oral bioavailability [49]. The poses of inhibitors were further refined by MD simulation to elucidate the backbone and side chain movements within the protein molecule. For backbone flip quantification in the hinge region, ψ angle of Met109 was exploited. At the start of each MD simulation, the NH group of Met109 was in the flipped state as indicated by the negative values of ψ_{109} angle. Later, ψ_{109} angle fluctuated around positive and negative values which unlike the apo conformation provide the space for **12f** positioning, enhanced by the electrostatic interactions of fluorine and bromine substituent on **12f** compound. At the end, the flip was induced again and H-bond was reformed between Gly110 and **12f** that was broken during ψ_{109} oscillations. No pronounced effect was seen on the DFG loop conformation for compounds **7a** and **8a**. The strength of interaction that leads to higher inhibitory activity increases with the increase in polarizability of halogen in the order Cl < Br < I $\approx$ H. The role of halogens with different protein systems is recently being investigated by two layer QM/MM ONIOM method [81]. The single point energy determination revealed that the halogen interaction is likely to be the same as that of hydrogen bonding. In our case, the developed models also support the effective halogen bonding, and in future would be use in rationale designing of potent halogenated drugs to deal with complex biological systems that have selectivity issues.

This computational progression has assisted us to fix the approximate crystal structure for docking, finding the most favorable ligand docked conformations, development of 3D-QSAR models for statistically refined descriptors of inhibitors, and computationally efficient way of dealing with receptor flexibility by MD simulation technique. Overall from our established CoMFA and CoMSIA models and MD simulations study, following important structural features should be considered into account when potency and selectivity would be the matter of concern: (1) the *N*-benzyl group should be electronegative with hydrogen bond acceptor at *para* position, (2) the benzyloxy group should have less and more steric bulk at *ortho* and *para* positions, respectively. The *para* moiety should be electronegative while the *ortho* substituent should have electropositive character, (3) the halogen isostere effect at C3 should have electropositive steric substituent. Since this model has inferred to be highly predictive on basis of significant statistical results obtained from 3D-QSAR, and their correlation with the MD simulations results has made it satisfactory to be extrapolated for the guidance of next generation p38α MAP kinase inhibitors.

Appendix A. Supplementary data

Supplementary data associated with this article can be found, in the online version, at doi:10.1016/j.jmgm.2012.02.003.

References

[1] R.J. Davis, Mol. Reprod. Dev. 42 (1995) 459–467.
[2] M.H. Cobb, E.J. Goldsmith, J. Biol. Chem. 270 (1995) 14843–14846.
[3] B. Dérijard, M. Hibi, I. Wu, T. Barrett, B. Su, T. Deng, M. Karin, R.J. Davis, Cell 76 (1994) 1025–1037.
[4] J. Han, J.D. Lee, L. Bibbs, R.J. Ulevitch, Science 265 (1994) 808–811.
[5] J. Raingeaud, S. Gupta, J.S. Rogers, M. Dickens, J. Han, R.J. Ulevitch, R.J. Davis, J. Biol. Chem. 270 (1995) 7420–7426.
[6] C.A. Dinarello, Curr. Opin. Immunol. 3 (1991) 941–948.
[7] M. Feldmann, F.M. Brennan, R.N. Maini, Cell 85 (1996) 307–310.
[8] G. Pearson, F. Robinson, T. Beers Gibson, B. Xu, M. Karandikar, K. Berman, M.H. Cobb, Endocr. Rev. 22 (2001) 153–183.
[9] R. Newton, N. Holden, BioDrugs 17 (2003) 113–129.
[10] W.P. Arend, J.M. Dayer, Arthritis Rheum. 33 (1990) 305–315.
[11] R.C. Newton, C.P. Decicco, J. Med. Chem. 42 (1999) 2295–2314.
[12] J.C. Lee, J.T. Laydon, P.C. McDonnell, T.F. Gallagher, S. Kumar, D. Green, D. McNulty, M.J. Blumenthal, J.R. Keys, Nature 372 (1994) 739–746.
[13] Y. Jiang, C. Chen, Z. Li, W. Guo, J.A. Gegner, S. Lin, J. Han, J. Biol. Chem. 271 (1996) 17920–17926.
[14] Z. Li, Y. Jiang, R.J. Ulevitch, J. Han, Biochem. Biophys. Res. Commun. 228 (1996) 334–340.
[15] Y. Jiang, H. Gram, M. Zhao, L. New, J. Gu, L. Feng, F. Di Padova, R.J. Ulevitch, J. Han, J. Biol. Chem. 272 (1997) 30122–30128.
[16] E. Herlaar, Z. Brown, Mol. Med. Today 5 (1999) 439–447.
[17] J.C. Lee, S. Kumar, D.E. Griswold, D.C. Underwood, B.J. Votta, J.L. Adams, Immunopharmacology 47 (2000) 185–201.
[18] G.S. Firestein, J.M. Alvaro-Gracia, R. Maki, J.M. Alvaro-Garcia, J. Immunol. 144 (1990) 3347–3353.
[19] P. Rutgeerts, G. D'Haens, S. Targan, E. Vasiliauskas, S.B. Hanauer, D.H. Present, L. Mayer, R.A. Van Hogezand, T. Braakman, K.L. DeWoody, Gastroenterology 117 (1999) 761–769.
[20] M.J. Elliott, R.N. Maini, M. Feldmann, J.R. Kalden, C. Antoni, J.S. Smolen, B. Leeb, F.C. Breedveld, J.D. Macfarlane, J.A. Bijl, Lancet 344 (1994) 1105–1110.
[21] M.J. Elliott, R.N. Maini, M. Feldmann, A. Long-Fox, P. Charles, J.A. Bijl, J.N. Woody, Lancet 344 (1994) 1125–1127.
[22] E.C.C. Rankin, E.H.S. Choy, D. Kassimos, G.H. Kingsley, A.M. Sopwtth, D.A. Isenberg, G.S. Panayi, Rheumatology 34 (1995) 334–342.
[23] H.M. Van Dullemen, S.J.H. van Deventer, D.W. Hommes, H.A. Bijl, J. Jansen, G.N.J. Tytgat, J. Woody, Gastroenterology 109 (1995) 129–135.
[24] L.W. Moreland, S.W. Baumgartner, M.H. Schiff, E.A. Tindall, R.M. Fleischmann, A.L. Weaver, R.E. Ettlinger, S. Cohen, W.J. Koopman, K. Mohler, Engl. J. Med. 337 (1997) 141–147.
[25] G.L. Johnson, R. Lapadat, Science 298 (2002) 1911–1912.
[26] T.F. Gallagher, G.L. Seibel, S. Kassis, J.T. Laydon, M.J. Blumenthal, J.C. Lee, D. Lee, J.C. Boehm, S.M. Fier-Thompson, J.W. Abt, Bioorg. Med. Chem. 5 (1997) 49–64.
[27] N.J. Liverton, J.W. Butcher, C.F. Claiborne, D.A. Claremon, B.E. Libby, K.T. Nguyen, S.M. Pitzenberger, H.G. Selnick, G.R. Smith, A. Tebben, J. Med. Chem. 42 (1999) 2180–2190.
[28] J.C. Lee, S. Kassis, S. Kumar, A. Badger, J.L. Adams, Pharmacol. Ther. 82 (1999) 389–397.
[29] D.M. Goldstein, T. Gabriel, Curr. Top. Med. Chem. 5 (2005) 1017–1029.
[30] B. Testa, P. Jenner, Drug Metab. Rev. 12 (1981) 1–117.
[31] L. Revesz, F.E. Di Padova, T. Buhl, R. Feifel, H. Gram, P. Hiestand, U. Manning, A.G. Zimmerlin, Bioorg. Med. Chem. Lett. 10 (2000) 1261–1264.
[32] S.A. Laufer, G.K. Wagner, J. Med. Chem. 45 (2002) 2733–2740.
[33] C.J. McIntyre, G.S. Ponticello, N.J. Liverton, S.J. O'Keefe, E.A. O'Neill, M. Pang, C.D. Schwartz, D.A. Claremon, Bioorg. Med. Chem. Lett. 12 (2002) 689–692.
[34] J.C. Boehm, J.M. Smietana, M.E. Sorenson, R.S. Garigipati, T.F. Gallagher, P.L. Sheldrake, J. Bradbeer, A.M. Badger, J.T. Laydon, J.C. Lee, J. Med. Chem. 39 (1996) 3929–3937.
[35] S.A. Laufer, G.K. Wagner, D.A. Kotschenreuther, W. Albrecht, J. Med. Chem. 46 (2003) 3230–3244.
[36] M.A. Fabian, W.H. Biggs, D.K. Treiber, C.E. Atteridge, M.D. Azimioara, M.G. Benedetti, T.A. Carter, P. Ciceri, P.T. Edeen, M. Floyd, Nat. Biotechnol. 23 (2005) 329–336.
[37] M.W. Karaman, S. Herrgard, D.K. Treiber, P. Gallant, C.E. Atteridge, B.T. Campbell, K.W. Chan, P. Ciceri, M.I. Davis, P.T. Edeen, Nat. Biotechnol. 26 (2008) 127–132.

[38] C.E. Fitzgerald, S.B. Patel, J.W. Becker, P.M. Cameron, D. Zaller, V.B. Pikounis, S.J. O'Keefe, G. Scapin, Nat. Struct. Biol. 10 (2003) 764–769.

[39] J.E. Stelmach, L. Liu, S.B. Patel, J.V. Pivnichny, G. Scapin, S. Singh, C. Hop, Z. Wang, J.R. Strauss, P.M. Cameron, Bioorg. Med. Chem. Lett. 13 (2003) 277–280.

[40] S.T. Wrobleski, A.M. Doweyko, Curr. Top. Med. Chem. 5 (2005) 1005–1016.

[41] S.R. Natarajan, J.B. Doherty, Curr. Top. Med. Chem. 5 (2005) 987–1003.

[42] M. Huse, J. Kuriyan, Cell 109 (2002) 275–282.

[43] M.D. Jacobs, P.R. Caron, B.J. Hare, Proteins 70 (2008) 1451–1460.

[44] M. Vogtherr, K. Saxena, S. Hoelder, S. Grimme, M. Betz, U. Schieborr, B. Pescatore, M. Robin, L. Delarbre, T. Langer, Angew. Chem. Int. Ed. 45 (2006) 993–997.

[45] T. Frembgen-Kesner, A.H. Elcock, J. Mol. Biol. 359 (2006) 202–214.

[46] C.D. Mol, D. Fabbro, D.J. Hosfield, Curr. Opin. Drug Discov. 7 (2004) 639–648.

[47] Z.A. Knight, K.M. Shokat, Chem. Biol. 12 (2005) 621–637.

[48] Y. Liu, N.S. Gray, Nat. Chem. Biol. 2 (2006) 358–364.

[49] S.R. Selness, R.V. Devraj, J.B. Monahan, T.L. Boehm, J.K. Walker, B. Devadas, R.C. Durley, R. Kurumbail, H. Shieh, L. Xing, Bioorg. Med. Chem. Lett. 19 (2009) 5851–5856.

[50] G.M. Sperandio da Silva, C.M.R. Sant'Anna, E.J. Barreiro, Bioorg. Med. Chem. 12 (2004) 3159–3166.

[51] P. Lan, Z.J. Huang, J.R. Sun, W.M. Chen, Int. J. Mol. Sci. 11 (2010) 3357–3374.

[52] M.R. Shashi Nayana, Y.N. Sekhar, N. Siva Kumari, S.K. Mahmood, M. Ravikumar, Eur. J. Med. Chem. 43 (2008) 1261–1269.

[53] R. Sarma, S. Sinha, M. Ravikumar, M.K. Kumar, S. Mahmood, Internet Electr. J. Mol. Des. 7 (2008) 38–46.

[54] G.K. Ravindra, G. Achaiah, G.N. Sastry, Eur J. Med. Chem. 43 (2008) 830–838.

[55] Z. Ul-Haq, I. Sadaf, Med. Chem. 5 (2009) 50–65.

[56] H.Z. Ul, R. Uddin, L.K. Wai, A. Wadood, N.H. Lajis, J. Mol. Model. (2010) (Epub ahead of print).

[57] Z. Ul-Haq, A. Wadood, R. Uddin, J. Enzym. Inhib. Med. Chem. 24 (2009) 272–278.

[58] R. Uddin, H. Yuan, P.A. Petukhov, M.I. Choudhary, J.D. Madura, J. Chem. Inf. Model. 48 (2008) 1092–1103.

[59] SYBYL Molecular Modeling Software, Tripos Associated Ltd., St. Louis, MO.

[60] J. Gasteiger, M. Marsili, Tetrahedron 36 (1980) 3219–3228.

[61] M. Clark, R.D. Cramer III, N. Van Opdenbosch, J. Comp. Chem. 10 (1989) 982–1012.

[62] R. Fletcher, M.J.D. Powell, Comput. J. 6 (1963) 163–168.

[63] M.L. Verdonk, J.C. Cole, M.J. Hartshorn, C.W. Murray, R.D. Taylor, Proteins: Struct. Funct. Bioinform. 52 (2003) 609–623.

[64] D.C. Richard Iii, E.P. David, D.B. Jeffrey, J. Am. Chem. Soc. 110 (1988) 5959–5967.

[65] G. Klebe, U. Abraham, T. Mietzner, J. Med. Chem. 37 (1994) 4130–4146.

[66] G. Klebe, U. Abraham, J. Comput-Aided Mol. Des. 13 (1999) 1–10.

[67] L. Ståhle, S. Wold, J. Chemometr. 1 (1987) 185–196.

[68] V.N. Viswanadhan, A.K. Ghose, G.R. Revankar, R.K. Robins, J. Chem. Inf. Model. 29 (1989) 163–172.

[69] S. Wold, Technometrics 20 (1978) 397–405.

[70] T.A. Darden, T.E. Cheatham III, C.L. Simmerling, J. Wang, R.E. Duke, R. Luo, M. Crowley, R.C. Walker, W. Zhang, K.M. Merz, B. Wang, S. Hayik, A. Roitberg, G. Seabra, I. Kolossvaĭry, K.F. Wong, F. Paesani, J. Vanicek, X. Wu, S.R. Brozell, T. Steinbrecher, H. Gohlke, L. Yang, C. Tan, J. Mongan, V. Hornak, G. Cui, D.H. Mathews, M.G. Seetin, C. Sagui, V. Babin, P.A. Kollman, AMBER 10, University of California, San Francisco, 2008.

[71] J. Wang, W. Wang, P.A. Kollman, D.A. Case, J. Mol. Graph Model. 25 (2006) 247–260.

[72] J. Wang, R.M. Wolf, J.W. Caldwell, P.A. Kollman, D.A. Case, J. Comput. Chem. 25 (2004) 1157–1174.

[73] U. Essmann, L. Perera, M.L. Berkowitz, T. Darden, H. Lee, L.G. Pedersen, J. Chem. Phys. 103 (1995) 8577–8593.

[74] J.P. Ryckaert, G. Ciccotti, H.J.C. Berendsen, J. Comput. Phys. 23 (1977) 327–341.

[75] H.J.C. Berendsen, J.P.M. Postma, W.F. van Gunsteren, A. DiNola, J.R. Haak, J. Chem. Phys. 81 (1984) 3684.

[76] W. Humphrey, A. Dalke, K. Schulten, J. Mol. Graph 14 (1996) 33–38.

[77] E.F. Pettersen, T.D. Goddard, C.C. Huang, G.S. Couch, D.M. Greenblatt, E.C. Meng, T.E. Ferrin, J. Comput. Chem. 25 (2004) 1605–1612.

[78] K.P. Wilson, M.J. Fitzgibbon, P.R. Caron, J.P. Griffith, W. Chen, P.G. McCaffrey, S.P. Chambers, M.S.S. Su, J. Mol. Biol. 271 (1996) 27696–27700.

[79] A.C. Wallace, R.A. Laskowski, J.M. Thornton, Protein Eng. Des. Sel. 8 (1995) 127–134.

[80] S.C. Karcher, S.A. Laufer, Curr. Med. Chem. 9 (2009) 655–676.

[81] Y. Lu, T. Shi, Y. Wang, H. Yang, X. Yan, X. Luo, H. Jiang, W. Zhu, J. Chem. Inf. Model. 52 (2009) 2854–2862.